Computers in Biology and Medicine 170 (2024) 107996

Contents lists available at ScienceDirect

Computers in Biology and Medicine

journal homepage: www.elsevier.com/locate/compbiomed

FFCM-MRF: An accurate and generalizable cerebrovascular segmentation pipeline for humans and rhesus monkeys based on TOF-MRA

Yue Cui [a,b,1,**], Haibin Huang [a,b,1], Jialu Liu [a,b], Mingyang Zhao [c], Chengyi Li [a,b], Xinyong Han [a,b], Na Luo [d], Jinquan Gao [f,g], Dong-Ming Yan [b,e], Chen Zhang [h], Tianzi Jiang [b,d,i], Shan Yu [a,b,*]

[a] Laboratory of Brain Atlas and Brain-inspired Intelligence, Institute of Automation, Chinese Academy of Sciences, Beijing, China
[b] School of Artificial Intelligence, University of Chinese Academy of Sciences, Beijing, China
[c] Hong Kong Institute of Science & Innovation, Chinese Academy of Sciences, Hong Kong, China
[d] Brainnetome Center, Laboratory of Brain Atlas and Brain-inspired Intelligence, Institute of Automation, Chinese Academy of Sciences, Beijing, China
[e] State Key Laboratory of Multimodal Artificial Intelligence Systems (MAIS), Institute of Automation, Chinese Academy of Sciences, Beijing, China
[f] Model R&D Center, Beijing Life Biosciences Company Limited, Beijing, China
[g] Technology Management Center, SAFE Pharmaceutical Technology Company Limited, Beijing, China
[h] Department of Neurobiology, School of Basic Medical Sciences, Beijing Key Laboratory of Neural Regeneration and Repair, Advanced Innovation Center for Human Brain Protection, Capital Medical University, Beijing, China
[i] Research Center for Augmented Intelligence, Zhejiang Lab, Hangzhou, China

ARTICLE INFO

Keywords:
Cerebral vessels
Generalization
Markov random field
Segmentation
TOF-MRA
Unsupervised learning

ABSTRACT

Purpose: Cerebrovascular segmentation and quantification of vascular morphological features in humans and rhesus monkeys are essential for prevention, diagnosis, and treatment of brain diseases. However, current automated whole-brain vessel segmentation methods are often not generalizable to independent datasets, limiting their usefulness in real-world environments with their heterogeneity in participants, scanners, and species.

Materials and methods: In this study, we proposed an automated, accurate and generalizable segmentation method for magnetic resonance angiography images called FFCM-MRF. This method integrated fast fuzzy c-means clustering and Markov random field optimization by vessel shape priors and spatial constraints. We used a total of 123 human and 44 macaque MRA images scanned at 1.5 T, 3 T, and 7 T MRI from 9 datasets to develop and validate the method.

Results: FFCM-MRF achieved average Dice similarity coefficients ranging from 69.16 % to 89.63 % across multiple independent datasets, with improvements ranging from 3.24 % to 7.3 % compared to state-of-the-art methods. Quantitative analysis showed that FFCM-MRF can accurately segment major arteries in the Circle of Willis at the base of the brain and small distal pial arteries while effectively reducing noise. Test-retest analysis showed that the model yielded high vascular volume and diameter reliability.

Conclusions: Our results have demonstrated that FFCM-MRF is highly accurate and reliable and largely independent of variations in field strength, scanner platforms, acquisition parameters, and species. The macaque MRA data and user-friendly open-source toolbox are freely available at OpenNeuro and GitHub to facilitate studies of imaging biomarkers for cerebrovascular and neurodegenerative diseases.

1. Introduction

The structural and functional integrity of blood vessels is essential to normal functioning of the brain, which relies highly on a complex and well-regulated vascular network to ensure an adequate supply of blood and meet its high demand for neural activity and metabolism. As a

* Corresponding author
** Corresponding author
E-mail addresses: yue.cui@nlpr.ia.ac.cn (Y. Cui), shan.yu@nlpr.ia.ac.cn (S. Yu).
[1] Yue Cui and Haibin Huang contributed equally to this work.

https://doi.org/10.1016/j.compbiomed.2024.107996
Received 4 October 2023; Received in revised form 14 December 2023; Accepted 13 January 2024
Available online 17 January 2024
0010-4825/© 2024 Elsevier Ltd. All rights reserved.

result, blood flow deficiencies and pathological changes in cerebral vessels can affect brain function and contribute to cerebrovascular diseases, such as stroke, aneurysms, and arteriovenous abnormalities, as well as neurodegenerative disorders, such as Alzheimer's disease [1]. The rhesus monkey (*Macaca mulatta*) is a commonly used animal model due to its genetic, brain structural, and behavioral similarities to humans [2]. A comprehensive delineation and reconstruction of the three-dimensional intracranial vessels for humans and nonhuman primates, along with a quantification of vascular morphological features, could provide insights into the impact of vascular changes on brain health. These may be beneficial for the prevention, diagnosis, and treatment of diseases associated with vascular dysfunction and cognitive decline.

Three-dimensional time-of-flight magnetic resonance angiography (TOF-MRA) is a noninvasive imaging technique for intracranial arterial (and some venous) vessels that is widely used in cerebrovascular clinical and scientific research. Deep learning techniques, such as U-Net and Transformer, have recently attracted interest in isolating vessels from brain tissues [3–8]. For instance, the nnU-Net framework, proposed by Isensee et al. [4], is currently regarded as the state-of-the-art network for biomedical image segmentation. In the field of vascular segmentation, Livne et al. used 2D U-Net for the first time to segment brain vessels and outperformed traditional graph-cuts method [3]. ER-Net is a neural network model based on the encoder-decoder framework, specifically designed for the purpose of cerebrovascular segmentation [7]. Similarly, CS^2-Net is a curvilinear structure segmentation network that incorporates spatial attention and channel attention mechanisms in both the encoder and decoder modules [8]. In addition, Chen et al. [6] proposed a generative consistency-based semi-supervised (GCS) model for cerebrovascular segmentation. This model integrates a Transformer architecture [9] and reconstruction consistency to improve the texture representation of the model. However, deep learning requires high-quality ground truth labels obtained via meticulous, voxel-wise manual delineation. This procedure is expensive in terms of time and manpower, dependent on highly trained and experienced experts, and prone to inter-expert variability [10]. In addition, deep learning models usually rely on large and heterogeneous training sets with high-quality annotations to prevent overfitting and ensure good performance on independent datasets. However, manual labeling of the whole brain's sophisticated and complex vasculature network is costly and prone to inter-annotator variability. As a result, publicly available high-quality annotated angiography datasets are limited for humans. Furthermore, to the best of our knowledge, there are no open-access TOF-MRA data and annotations for nonhuman primates. Therefore, the lack of enough high-quality annotated datasets limits the applicability of deep models for cerebrovascular segmentation in humans and macaques. In contrast, unsupervised learning methods, such as finite mixture model, capture intrinsic patterns of vessels based on the global properties of the intensity distributions in TOF-MRA [11,12]. Such methods are independent of ground truth labels and adapted to relatively small datasets. However, finite mixture models, which rely on expectation maximization algorithm to estimate parameters, are prone to parameter drifting due to unbalanced proportions of vascular (~5 %) and nonvascular (~95 %) voxels [13]. Fuzzy c-means (FCM) clustering is one of the most widely used techniques in the field of medical image segmentation and can provide better results than finite mixture models [14]. FCM clustering method has been widely used in previous image segmentation studies. For example, Krinidis et al. introduced a robust segmentation method called fuzzy local information c-means clustering (FLICM), which incorporates local spatial and gray level constraints to improve noise tolerance [15]. In addition, an improved fuzzy c-means clustering (IFCM) method was developed to enhance segmentation performance by leveraging the relative location and intensity of neighboring pixels [16]. However, relying solely on FCM clustering for vessel segmentation in TOF-MRA images may lead to the presence of vascular fragments and non-vessel noises because it does not take into account the spatial continuity and morphological characteristics of vessels [17]. To address these limitations, researchers have incorporated vessel enhancement techniques, such as Frangi's filter [17] and Hessian matrix eigenvalues [18] into the objective function of FCM. However, vessel-enhanced images often introduce excessive pseudo vessels, which generally result in inaccurate vessel segmentation. In contrast, the integration of Markov random field (MRF) with the statistical model allows for spatial similarity constraints among neighboring voxels and tubular structure priors characterized by improved vessel enhancement method [19], thereby suppressing non-vessel noises while enhancing the continuity of the segmented vessels [11]. Inspired by related studies, we creatively designed an MRF energy function after the FFCM segmentation stage, incorporating vessel shape and local characteristics constraints in a three-dimensional neighborhood system.

Vessels are spatially heterogeneously distributed across the brain to meet distinct energy and neural interaction requirements [20,21]. Various vascular features including volume, length, and diameter based on a three-dimensional segmentation of vessels provide qualitative mapping and analyses of morphological characteristics, thereby enabling a better understanding of brain structural and functional organization. Most studies have focused on the location and morphology of the Circle of Willis [22,23] and distal arteries [20] in humans. Although vascular patterns have become available through human studies, the information about the segmentation, extraction, and quantification of cerebral vessels in rhesus monkeys is still quite limited. There is also a lack of rhesus monkey angiography datasets to promote progress in comparative neuroscience and translational medicine.

In the present study, we developed a novel framework called fast fuzzy c-means clustering combined with MRF optimization (FFCM-MRF) for cerebrovascular segmentation on TOF-MRA images. Tubular-shaped priors of blood vessels and spatial neighborhood information were leveraged by MRF optimization process to reduce segmentation noise and enhance spatial continuity of the segmented vessels. The proposed method was validated on multiple independent human and macaque datasets and compared with state-of-the-art methods. Vascular volume density and diameter features were then extracted and analyzed for humans and macaques. We also developed a user-friendly MATLAB toolbox for vessel segmentation and quantification based on FFCM-MRF framework.

2. Materials and methods

2.1. MRA datasets

A total of 123 human and 44 macaque MRA images scanned at 3 T and 7 T MRI from 9 datasets were used to develop and validate FFCM-MRF. Human MRA data were taken from the publicly available MIDAS, BraVa (http://cng.gmu.edu/brava/home.php), CHUV (https://openneuro.org/datasets/ds003949/versions/1.0.1), ADAM (https://adam.isi.uu.nl), Forrest (https://www.studyforrest.org), and Midnight Scan Club (MSC, https://legacy.openfmri.org/dataset/ds000224/) datasets. The MIDAS database was released by the CASILab at the University of North Carolina at Chapel Hill. The present study included 54 MRA images with voxel-wise ground truth labels, of which 20 were manually labeled by Hilbert et al. [24], and 3 4 were released by the CASILab (https://public.kitware.com/Wiki/TubeTK/Data). Note that the ground truth labels only focused on arteries, but we also included veins, such as the venous sinus, due to their prominence in MRA images. Subsets of ADAM, BraVa, and CHUV were used as independent datasets to validate the FFCM-MRF. The Forrest dataset comprises 7 T high field strength high-resolution MRA images from 20 participants. Of these images, 14 were labeled by SMILE-UHURA Challenge 2023 (https://www.soumick.com/en/uhura/). The MRA acquisition of Forrest dataset was performed with partial brain coverage and high resolution. Test-retest validation was performed using the MSC dataset, which included four repeated MRA scans for each of 10

participants.

36 Macaque MRA images were acquired from a 3 T Siemens Prisma scanner in Wuhan (Maca-WH), 4 were acquired from a 3 T Siemens Prisma scanner from the Institute of Biophysics, Chinese Academy of Sciences in Beijing (Maca-BJ), and 4 were obtained from a 7 T MAGNETOM Terra scanner (Maca-7T) at the same institute. The monkeys were anesthetized with an intramuscular injection of Zoletil 50 (10 mg/kg) before scanning and were maintained under anesthesia using 0.5 % isoflurane in oxygen during image acquisition [25]. The animals were placed in a sphinx position during the scan, with an MRI-compatible stereotaxic frame optimized for the NHP head. Ground truth labels for ADAM, BraVa, CHUV, and macaques were labeled by a trained annotator and two students (authors H.H. and J.L.). See Tables 1 and 2 for subject details and references for acquisition parameters. This study was approved by the Institutional Review Board/Ethics Committee of Chinese Academy of Sciences Institute of Automation. To the best of our knowledge, the present study leveraged relatively more and diverse datasets with various field strengths (7T, 3T and 1.5T), scanner types (Siemens and Philips), acquisition parameters, and species (humans and macaques) for generalizability and applicability analysis.

2.2. Automated cerebrovascular segmentation procedure

The automated cerebrovascular segmentation procedure consisted of three stages: MRA pre-processing, rudimentary segmentation using fast fuzzy c-means clustering, and MRF optimization using a neighborhood energy function. These stages are illustrated in Fig. 1 and described in detail below.

2.2.1. MRA pre-processing

The MRA images were skull stripped, denoised and bias field corrected in the pre-processing stage. Specifically, the MRA images were skull stripped using BET function [26] in FSL 6.0 for humans, and DeepBet [27] for macaques to remove non-brain tissues. BET uses a tessellated mesh to model the brain surface, which is allowed to deform according to various dynamic controlling terms until it reaches the brain edge. DeepBet is a U-Net model designed for brain extraction in non-human primates (NHPs). It was developed using transfer learning, where a U-Net model was pretrained on a large human dataset and then transferred and finetuned on NHP data. The extracted brains were carefully reviewed, and manually edited using ITK-SNAP (http://www.itksnap.org/pmwiki/pmwiki.php) if necessary. Brain extraction was followed by *DenoiseImage* and *N4BiasFieldCorrection* functions in ANTS for denoising and bias field correction. To mitigate the variability of intensity distributions across scanners and subjects, we used histogram specification to normalize these images (Supplementary Figure 1). Histogram specification is a technique used to adjust global contrast of an image by matching its histogram to a target histogram. Before applying histogram specification, the input intracranial TOF-MRA data were convolved with a $3 \times 3 \times 3$ Gaussian kernel to enhance the continuity of grayscale values as per [11]. Let w and z denote the grayscale values of the images before and after histogram specification, respectively. $p_w(w)$ and $p_z(z)$ are the probability density functions of the images before and after histogram specification, respectively. The cumulative distribution function H for w can be calculated by $H = T(w) = \int_0^w p_w(w)dw$, where T is the cumulative operator. The transformation function $G(z) = \int_0^z p_z(z)dz = H$ was obtained using target histogram $p_z(z)$. Let $G(z) = T(w)$, so z should satisfy the equation $z = G^{-1}(H) = G^{-1}(T(w))$. The histogram-aligned image (i.e., image after histogram specification) can be obtained by applying G^{-1} to all voxels in input (i.e., image before histogram specification) image. The target histogram was generated as follows. We first calculated the peak value of the histogram for each subject in the MIDAS dataset, and then identified the peak value that was most common among the histograms, and finally averaged the histograms with that peak value to obtain the target histogram. The histograms of all the subjects in MIDAS, BraVa, CHUV, ADAM, and Forrest were then matched to the target histogram established using MIDAS. For macaques, the target histogram was generated using the Maca-WH dataset, and then all the macaque MRA images were aligned to it.

Table 1
Subject demographics[a].

	Dataset	Subject number	Age (years)	Sex (F/M)
Humans	MIDAS	54	38.1 (12.3)	23/31
	BraVa	5	28.8 (8.9)	1/4
	CHUV	5	–	–
	ADAM	5	–	–
	Forrest	14	20–35	4/9
	MSC	10 (40 scans)	29.1 (3.2)	5/5
Macaques	Maca-WH	36	9.4 (4.0)	36/0
	Maca-BJ	4	4.0 (0.6)	4/0
	Maca-7T	4	4.5 (1.0)	4/0

[a] Age and sex information are not available for the ADAM and CHUV datasets. Values are mean (SD) for age except in the Forrest dataset, which uses a range.

2.2.2. Rudimentary segmentation using fast fuzzy c-means clustering

In the present study, fast FCM (FFCM) was used for rudimentary cerebrovascular segmentation. FCM is a data clustering technique in which voxels are grouped into some clusters based on fuzzy membership degrees. Differently from conventional FCM, the FFCM calculates the membership degree matrix and cluster centers based on the histogram rather than individual voxels to decrease the execution time for clustering [28]. As a result, the membership calculation was dramatically reduced from an average of more than 6,500k to 0.5 - 1k values. The main steps for the FFCM algorithm are as follows.

Let $Y = \{y_1, y_2, \cdots, y_S\}$ denote an MRA image with S histogram bins to be partitioned into $C(2 \le C \le S)$ clusters, where y_i represents the intensity of voxels in the histogram bin $i \in 1, \ldots, S$, and H_i is the frequency of the intensity level at i. The number of histogram bins was set to the maximum intensity value of the image, and the bin width was set to the minimum integer of 1. Note that in conventional FCM, y_i represents the intensity of each voxel in TOF-MRA instead of the histogram of the image.

First, histogram-based k-means clustering was used to generate initial cluster centers $Z_k, k = 1, \cdots, C$ for FFCM. The membership degree matrix was then calculated as follows:

$$u_{ki} = \frac{1}{\sum_{l=1}^{C} \left(\frac{\|y_i - Z_k\|}{\|y_i - Z_l\|} \right)^{2/(m-1)}}, \tag{1}$$

where $m\,(m > 1)$ is the fuzzy factor, controlling the fuzziness of the resulting partition. The cluster centers were calculated by:

$$Z_k = \frac{\sum_{i=1}^{S} u_{ki}^m y_i H_i}{\sum_{i=1}^{S} u_{ki}^m H_i}, \tag{2}$$

The algorithm iteratively updates the membership degrees u_{ki} and cluster centers $Z_k, (k = 1, 2, \cdots, C)$ according to Eq 1 and Eq 2, until convergence with $\max \left| Z_k^t - Z_k^{t-1} \right| < \varepsilon$, where ε is a user-defined threshold. Note that in conventional FCM, the calculation of Z_k does not utilize the frequency H for voxels with the same intensity. Instead, it processes each voxel separately, resulting in a substantial computation load for 3D TOF-MRA images. At the end of the iterations, a membership degree matrix with a size of $S \times C$ was obtained, which contains the membership degrees for voxels at each intensity level, indicating the likelihood of the voxels belonging to each cluster.

Note that when $\|y_i - Z_k\| = 0$, there may arise a singularity problem since the membership degree $u_{ki} = 1$, which leads to the failure of the

Table 2
TOF-MRA acquisition parameters.

	Dataset	Scanner	Magnetic field strength (T)	Voxel resolution (mm^3)	TR/TE (ms)	Flip angle (degrees)	Field of view (mm^3)
Humans	MIDAS	Siemens	3	0.51 × 0.51 × 0.80	35/3.56	22	180 × 228 × 141
	BraVa	Siemens	3	0.62 × 0.62 × 0.62	24/4.85	18	179 × 198 × 123
	CHUV	Siemens Verio/Philips Intera	3	0.47 × 0.47 × 0.7 /0.41 × 0.41 × 0.55	22/3.95	18	164 × 210 × 112 /210 × 210 × 77
	ADAM	Philips	1.5	0.31 × 0.31 × 0.70 /0.39 × 0.39 × 0.5	25/6.91	–	159 × 159 × 70 /200 × 200 × 69
	Forrest	Siemens MAGNETOM	7	0.30 × 0.30 × 0.30	24/3.84	8	192 × 144 × 49
	MSC	Siemens Tim Trio	3	0.625 × 0.625 × 1	25/3.34	20	181 × 200 × 268
Macaques	Maca-WH	Siemens Prisma	3	0.50 × 0.50 × 0.50	20/3.69	18	106 × 128 × 47
	Maca-BJ	Siemens Prisma	3	0.21 × 0.21 × 0.32	23/3.81	18	160 × 129 × 54
	Maca-7T	Siemens MAGNETOM	7	0.19 × 0.19 × 0.30	24/5.83	23	120 × 90 × 50

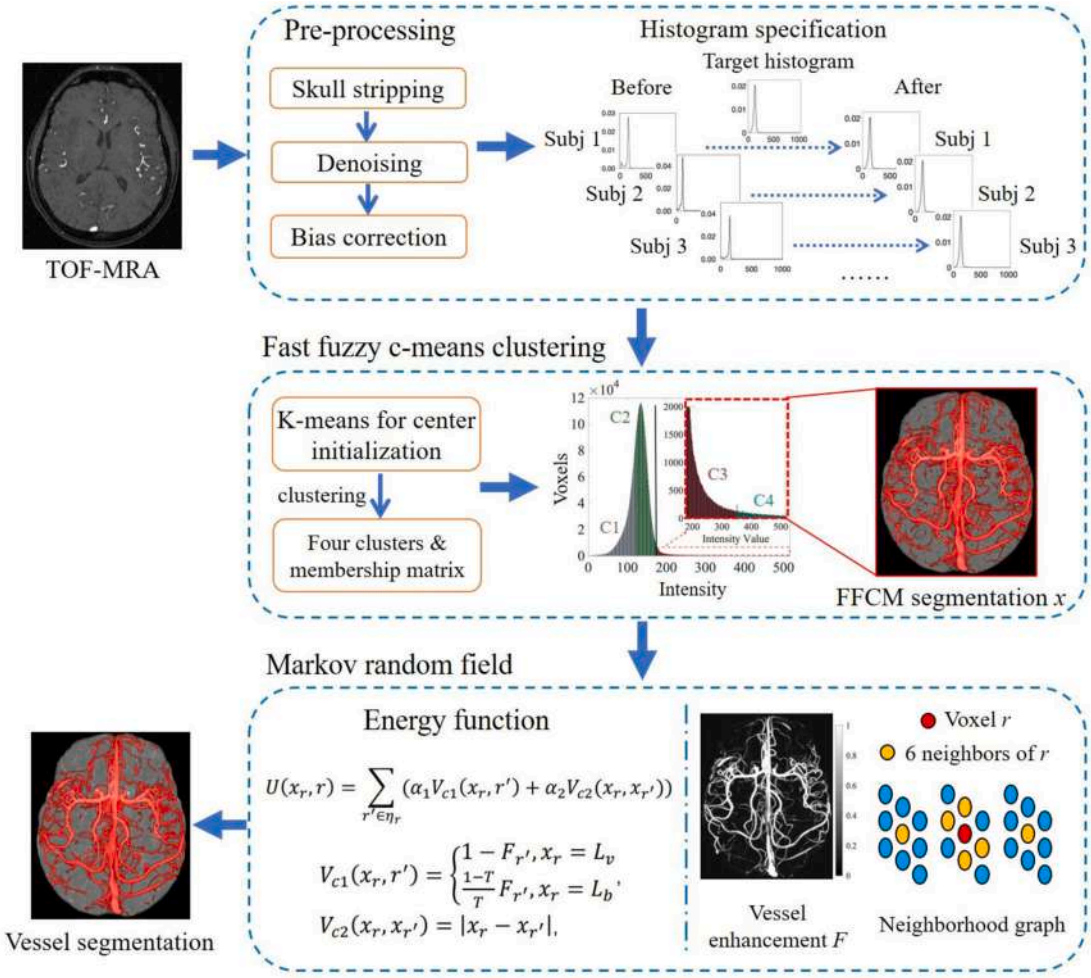

Fig. 1. Flowchart of the cerebrovascular segmentation using fast fuzzy c-means clustering combined with Markov random field optimization by spatial and shape constraints.

subsequent MRF process. To solve this problem, the membership degree matrix was clipped within the range of 0 and 1 by:

$$u_{ki} = \frac{1}{1 + \|y_i - Z_k\|^{1/(m-1)}}, \tag{3}$$

Finally, each voxel r in TOF-MRA can be labeled with 1 (vessel) or 0 (background) as follows:

$$x_r = \begin{cases} 1, o_r \geq 3 \\ 0, o_r < 3 \end{cases}, r = 1, \cdots, N, \tag{4}$$

where x_r represents the label of current voxel r, o_r is the highest membership degree defined by:

$$o_r = \underset{k}{\text{argmax}}\, u_{kr}, r = 1, 2, \cdots, N, \tag{5}$$

where u_{kr} denotes the corresponding membership degree of voxel r with cluster k (identical with u_{ki}, i.e., voxel r within histogram bin i), and N is the number of intracranial voxels.

Experimentally, we compared the segmentation results obtained from three- and four-cluster FFCM, and found that when the cluster number $C = 4$, voxels in the first and second clusters corresponded to cerebrospinal fluid and brain tissues, respectively, while voxels in the third and fourth clusters corresponded to cerebral vessels. Since four-

cluster FFCM provided more vessels, it was adopted for rudimentary segmentation. (Supplementary Figure 2).

2.2.3. MRF optimization

Due to the reliance solely on intensity information, the rudimentary segmentation results obtained from the FFCM model often exhibit noise and fail to capture vascular structures in regions with low contrast within the image. In order to further optimize the rudimentary segmentation results, spatial constraints among neighboring voxels were necessary for constructing an MRF model. In MRF theory, image segmentation involves estimating the labels of voxels through a combination of low- and high-level random processes. The low-level process models observed variable set $Y = \{y_1, y_2, \cdots, y_N\}$, which represents voxel intensities, are conditionally independent. In the present study, the low-level process was implemented by FFCM, which provided membership degrees and initial label fields for the high-level process. The high-level process models latent label variable set $X = \{x_1, x_2, \cdots, x_N\}$ with values from the label set $L = \{L_v, L_b\}$, representing vessel and non-vessel (background) voxels, respectively. According to the Bayesian rule, the optimal label for voxel r is obtained through maximizing its posterior probability:

$$max_{x_r \in L}\, p(x_r = L_*|y_r) \propto max_{x_r \in L}\, p(y_r|x_r = L_*) p(x_r = L_*) \tag{6}$$

The first term $p(y_r|x_r = L_*)$, which is the low-level MRF process for likelihood probability, is derived from the membership degrees through FFCM in the present study. This membership degrees can be denoted as u_{vr} and u_{br} for vessels and non-vessels, respectively, and calculated as follows:

$$\begin{cases} p(y_r|x_r = L_v) = u_{vr} = \dfrac{\sum_{k=3}^{4} w_k u_{kr}}{\sum_{k=3}^{4} w_k} \\ p(y_r|x_r = L_b) = u_{br} = \dfrac{\sum_{k=1}^{2} w_k u_{kr}}{\sum_{k=1}^{2} w_k} \end{cases} \tag{7}$$

where w_k denotes the proportion of vessel voxels in cluster k that was determined in the FFCM segmentation.

The prior probability of label variables $p(x_r = L_*)$ in the high-level Markov process can be modeled as the Gibbs distribution according to Hammersley-Clifford Theorem [29] as follows:

$$\begin{aligned} p(x_r = L_*) &= \exp(-\beta U(x_r = L_*))/M, \\ M &= \sum\nolimits_{L_* \in L} \exp(-\beta U(x_r = L_*)), \end{aligned} \tag{8}$$

where $U(x_r = L_*)$ is an energy function, the parameter β describes the strength of the interaction between pair-wise neighboring voxels. In the present study, we proposed a new energy function that integrates labels and tubular structure priors into a six-neighborhood system, which enables modeling spatial constraints among neighboring voxels to reduce segmentation noise and enhance spatial continuity of the segmented vessels. The energy function was defined as follows:

$$U(x_r, r) = \sum_{r' \in \eta_r} (\alpha_1 V_{c1}(x_r, r') + \alpha_2 V_{c2}(x_r, x_{r'})), \tag{9}$$

where x_r represents the label of the current voxel r, $x_{r'}$ represents the label of one of the adjacent voxels of r, and η_r is the set of six spatial neighbors of r. The initial setting of x is segmentation results by FFCM, and x is then iteratively updated by MRF. Both α_1 and α_2 were set to 0.5 in the present study [11]. V_{c1} and V_{c2} are defined as follows:

$$V_{c1}(x_r, r') = \begin{cases} 1 - F_{r'}, x_r = L_v \\ \dfrac{1 - T}{T} F_{r'}, x_r = L_b \end{cases}, \tag{10}$$

$$V_{c2}(x_r, x_{r'}) = |x_r - x_{r'}|, \tag{11}$$

where $F\ (0 \le F \le 1)$ is the Hessian-based multi-scale filtering response image for vessel enhancement, which can effectively highlight tubular structure and suppress non-vascular tissues [19]. T is the threshold that defines the vessel voxels in F and can be calculated by

$$T = F_{\left(\sum_{r=1}^{N} x_r\right)}, \tag{12}$$

where $F_{(n)}$ represents the nth highest value among all the voxel response values in F.

Combining Equations (6)–(8) together, the posterior probabilities of vessel and non-vessel voxels can be expressed as:

$$\begin{cases} p(x_r = L_v|y_r) \propto u_{vr} \exp(-\beta U(x_r = L_v, r)) \\ p(x_r = L_b|y_r) \propto u_{br} \exp(-\beta U(x_r = L_b, r)) \end{cases} \tag{13}$$

If a voxel meets $p(x_r = L_v|y_r) > p(x_r = L_b|y_r)$, it is considered a vascular voxel and thus the label was updated. The MRF optimization process is applied using iterated conditional modes [30] to iteratively update the labels until it reaches the maximum iteration (i.e., itermax). The algorithm of FFCM-MRF is shown in Algorithm 1.

Algorithm 1 Fast Fuzzy C-mean Markov Random Field (FFCM-MRF)

Input: MRA image Y, image histogram H, vessel enhancement image F
Output: MRA segmentation X

Fix C, m, *itermax*, stop criterion ϵ
Stage 1: FFCM
Initialize the cluster centers Z_k, $k = 1, ..., C$ using histogram based k-means
repeat
  Update membership matrix u_{ki}, $i = 1, ..., S$, according to Eq. (1)
  Update the cluster centers Z_k, $k = 1, ..., C$, according to Eq. (2)
  Calculate the stopping criterion $\Delta Z = max|Z_k^t - Z_k^{t-1}|$
until $(\Delta Z < \epsilon)$
Update the membership matrix u_{ki} according to Eq. (3)
Derive the membership value o_r according to Eq. (5)

# Get rudimentary segmentation x_r with C=4 according to Eq. (4)
if $o_r \ge 3$ **then**
  $x_r = 1$
else
  $x_r = 0$
end if

Stage 2: MRF
Initialize threshold T according to Eq. (12)
Initialize counter i to 0
repeat
  $i = i + 1$
  Calculate the first energy function V_{c1} according to Eq. (10)
  Calculate the second energy function V_{c2} according to Eq. (11)
  Calculate membership u_{vr} for vessel class according to Eq. (7)
  Calculate membership u_{br} for non-vessel class according to Eq. (7)
  Derive overall energy function $U(x_r, r)$ according to Eq. (9)
  Calculate $p(x_r = L_v|y_r)$ for vessel class according to Eq. (13)
  Calculate $p(x_r = L_b|y_r)$ for non-vessel class according to Eq. (13)

  # Refine segmentation according to maximum a posterior probability
  if $p(x_r = L_v|y_r) > p(x_r = L_b|y_r)$ **then**
    $x_r = L_v$
  else
    $x_r = L_b$
  end if
  Update threshold T according to Eq. (12)
until $(i =$ itermax$)$

We randomly selected 50 % of the participants from MIDAS to tune the parameters m and β by maximizing the Dice similarity coefficient (DSC), which evaluates the overlapping extent between segmentation and ground truth, and is defined as DSC $= 2TP/(2TP + FP + FN)$, where TP is the number of true positive voxels, FP is the number of false positive voxels and FN is the number of false negative voxels. Optimal parameters m and β were then applied to the whole MIDAS, as well as to the independent human (BraVa, CHUV, ADAM and Forrest) and macaque (Maca-WH, Maca-BJ and Maca-7T) datasets.

2.3. FFCM-MRF quantitative evaluation

The complete evaluation and validation of FFCM-MRF were based on the results from qualitative, quantitative, and test-retest reliability assessments. For quantitative analyses, the DSC, precision score, recall score, average Hausdorff distance (AHD) and ΔIslands metrics were used to evaluate the performance of each method. The precision score

measures the proportion of correctly segmented vascular voxels relative to the total number of segmented voxels, i.e., Precision = TP /(TP + FP). The recall score measures the proportion of correctly segmented vascular voxels relative to the number of voxels in the ground truth, i.e., Recall = TP /(TP + FN). AHD measures average Hausdorff distance between two binary volumes, i.e., segmentation and ground truth over all voxels. ΔIslands represents the absolute difference of connected vascular segments between the segmentation and the ground truth. A lower value of ΔIslands means a closer similarity in the connectivity characteristic of the cerebrovascular system between the segmentation and the ground truth. The Python package "connected-components-3d" configured with 26-connected neighborhood, was utilized to calculate connected vascular segments of binary segmentation map. In addition, an integrated rank was calculated for each method by taking the average of the method's rankings across all metrics. A smaller integrated rank indicates a higher overall performance for the method, as it suggests a better ranking across all evaluation metrics.

2.4. Comparisons with other state-of-the-art models

FFCM-MRF was compared with four state-of-the-art deep neural network models, nnU-Net [4], ER-Net [7], CS^2-Net [8] and GCS [6], as well as with three statistical models including IFCM [16], FLICM [15] and GMM-MRF [11]. The TOF-MRA images were pre-processed using skull stripping, denoising, bias field correction, and histogram specification before being used as input for these models. The nnU-Net model was trained for 1000 epochs, with 250 iterations per epoch. In each iteration, two patches of size 160 × 192 × 80 were randomly cropped from the volume, and at least one-third of the patches in each iteration were guaranteed to contain vessels to handle class imbalances. By default, nnU-Net resamples all images to the same target spacing, but for macaque MRA images with higher resolution compared to human images, resampling was not performed to avoid potential suboptimal segmentation performance. Stochastic gradient descent with Nesterov momentum (μ = 0.99) and an initial learning rate of 0.01 were used to learn network weights. ER-Net was trained for 200 epochs, with 250 iterations per epoch. In each iteration, a patch with a size of 96 × 96 × 96 was randomly cropped from the image, followed by a 90-degree rotation for data augmentation. The Adam optimizer and an initial learning rate of 0.0001, with a weight decay of 0.0005 were used for network optimization. CS^2-Net was trained for 200 epochs, with 250 iterations per epoch. In each iteration, two patches of size 128 × 128 × 128 were randomly cropped from the volume. The configuration of optimizer and learning rate for CS^2-Net were same as for ER-Net. GCS utilizes additional 182 unlabeled images from multiple datasets (MIDAS n = 55, BraVa n = 51, CHUV n = 55, ADAM n = 15 and Forrest n = 6) along with labeled images for training. The hyper-parameters used in GCS are consistent with those in Chen et al. [6], including randomly cropping patches of size 128 × 128 × 128 from the volumes and setting the maximum epoch to 20. Each epoch involves randomly cropping 10 patches from each volume (27 volume from MIDAS dataset), resulting in 135 iterations. Each iteration consists of 2 patches from labeled images and 2 patches from unlabeled images. The Adam optimizer and an initial learning rate of 0.005 were used to learn the network weights.

To ensure generalization and reduce variability, a 2-fold cross-validation was applied to these four deep neural network models using the MIDAS dataset. This involved randomly dividing the MIDAS dataset into two subsets: one for testing and the remaining one as training and validation data (80 % for training and 20 % for validation). This process was repeated twice, with each subset serving as the test data once. The final segmentation results for the MIDAS dataset were obtained by averaging the outputs of these two independent experiments. The model that performed better on the test set was selected as the optimal model and used for independent validation on all other datasets. The deep neural network models were all implemented using the Pytorch framework (v2.0.0) and trained on a high-performance server equipped with a single NVIDIA GeForce RTX 3090 GPU.

For IFCM and FLICM, the weighting exponent m and number of clusters C were set to the same values as we did for FFCM-MRF, to ensure a fair comparison. For GMM-MRF, we selected the same participants from MIDAS dataset as we did for FFCM-MRF to tune parameter β by maximizing the DSC. The optimal β obtained from this tuning process was then applied to all images in the MIDAS dataset as well as other independent datasets. Four statistical models were implemented using MATLAB2017b on a PC Intel(R) Xeon(R) Gold 5318Y CPU @2.10 GHz.

2.5. Test-retest reliability

For the reliability assessment, FFCM-MRF was applied to the human MIDNIGHT MSC database and rhesus monkey test-retest data. MSC database contains 10 participants with 4 MRAs for each participant. Rhesus monkey test-retest data consists of macaques M14 and M28. M14 was scanned twice using a 3 T S scanner, and M28 was scanned using 3 T and 7 T S scanners. In each image, the vascular volume density and average diameter of each region of interest (ROI) were computed according to the human [31] and macaque [32] Brainnetome atlases, which included 210 and 248 ROIs for human and macaque cortices, respectively. These ROIs were obtained by anatomical landmarks and structural connectivity profiles by diffusion MRI. Diameters were computed using the method introduced by Ref. [33], where the segmentation image was resampled to isotropic spacing, followed by skeletonization to obtain the centerline. The diameters were then calculated as the thickness of the maximum possible sphere fitting for each vessel along the centerline.

An intra-class correlation coefficient (ICC) was used to assess the reliability of the vascular volume density and diameter across scans in the MSC dataset. ICC estimates and their 95 % confidence intervals were computed based on a single rater/measurement, absolute agreement, two-way mixed effects model (ICC(3,1)). Diameters and ICC were calculated using SimpleITK and Pingouin Python packages, respectively. (Python 3.7.3, SimpleITK 2.3.1 and Pingouin v.0.3.11).

2.6. FFCM-MRF application

The group-averaged ROI-based vascular volume density and diameters were calculated for the subjects from the MIDAS (n = 54) and Maca-WH (n = 36) datasets based on the human and macaque Brainnetome atlases for cerebrovascular evolutionary comparisons. Specifically, each native TOF-MRA image was first linearly then nonlinearly warped to the structural template in atlas space. The derived transformation parameters were then used to warp vascular density and diameter measurements from native space to atlas space. The registration procedures were performed using Aladin and F3D tools from the NiftyReg package (https://sourceforge.net/projects/niftyreg/). The measurements in each volume-based ROI were averaged across subjects and then z-scored across cortex. The normalized measurements were assigned to surface-based atlas and visualized using Connectome Workbench (https://www.humanconnectome.org/software/connectome-workbench). In addition, voxelwise feature maps were computed inside the bounding boxes of 15- and 8-cube for humans and macaques, respectively, with each brain voxel as the center of the bounding box. The features within a bounding box were allocated to the voxel. Volume-based vascular density and diameter measurements were mapped to individual surfaces. Note the individual surfaces were constructed with native T1- and T2-weighted images using HCP pipeline for humans (https://github.com/Washington-University/HCPpipelines) and NHP pipeline for macaques (https://github.com/Washington-University/NHPPipelines), and then used a nonlinear registration to align with the MNI coordinate system. The surface-based measurements were averaged across subjects and then z-scored across cortex.

3. Results

3.1. Qualitative and quantitative assessment

Model training and test procedures for nnU-Net, ER-Net, CS^2-Net and GCS, and hyperparameter tuning for GMM-MRF and FFCM-MRF methods in the MIDAS dataset are presented in Supplementary Figures 3 and 4. For GMM-MRF, the optimal β was 0.1. For FFCM-MRF, the optimal β was between 0.001 and 0.01, and m was between 1.1 and 1.9; so we set β to 0.01 and m to 1.7 for all datasets. The convergence process of FFCM and the impact of the number for FFCM-MRF were analyzed on MIDAS dataset, as depicted in Supplementary Figure 4C. We observed that the model achieved convergence within 10 iterations. Beyond these iterations, the model's performance remained stable, but the computational time increased. The complete quantitative results for each method on multiple datasets are shown in Fig. 2 and Table 3. DSC is widely used to measure spatial overlapping extent between the segmentation and ground truth labels, and has been deemed to the most important index reflecting the model performance in previous vessel segmentation studies [6,23]. Therefore, we determined that the model has the best performance based on the highest DSC in the present study. Specifically, on the MIDAS dataset, nnU-Net, ER-Net and CS^2-Net outperformed FFCM-MRF, with an improvement of 5.71 %, 1.91 % and 4.34 % in DSC, respectively. While for independent human and macaque datasets, FFCM-MRF outperformed other methods by an average increase ranging from 3.43 % to 7.3 % in DSC. Compared with nnU-Net, FFCM-MRF achieved an improvement in DSC ranging from 0.16 % to 6.74 % across independent datasets. The superiority of FFCM-MRF was consistently replicable in comparison to nnU-Net trained with different epochs, ranging from 100 to 1000 epochs (Supplementary Figure 5). We observed that the integrated rank of FFCM-MRF was the top compared with other methods across seven independent datasets, suggesting that FFCM-MRF is a competitive model. In addition, no significant correlation ($r = 0.03$, $p = .951$) was observed between the average number of intracranial voxels and the DSC scores across all datasets, suggesting that the variation of MRA image sizes does not have impact on our model's performance (Supplementary Figure 6).

The detailed qualitative analysis of the segmentation results on MIDAS dataset using state-of-the-art methods is shown in Fig. 3. It is worth noting that small distal vessels were often ignored by annotators, while the proposed FFCM-MRF was superior in detecting these vessels (see also Supplementary Figure 7). Qualitative analysis of the segmentation results on new images from the independent datasets showed that the proposed FFCM-MRF is capable of segmenting large blood vessels, including the internal carotid arteries (ICA, Fig. 4B) and small distal arteries (Fig. 4). In addition, our method is more robust to noise than GMM-MRF because it benefits from the more useful Markov optimization process.

Detailed comparisons between nnU-Net and FFCM-MRF showed that nnU-Net exhibited poorer detection of vessels near the edge of the brain, including Circle of Willis (CW) arteries located at the base of the brain and small distal arteries that cover the cerebral cortical surface (Fig. 5A). Because the CW plays a vital role in brain health and provides an anastomotic connection between the anterior and posterior circulations and between the left and right hemispheres, we labeled the CW arteries by overlaying the vessel labels and CW segmentation results obtained from an automated CW segmentation pipeline [23]. The obtained CW ground truth labels were used to calculate the detection rates, which measured the proportion of correct segmentation achieved for each CW artery, for both nnU-Net and FFCM-MRF (Fig. 5 and Supplementary Table 2). We observed that the detection rates of the CW arteries using FFCM-MRF outperformed nnU-Net for most of the large arteries on MIDAS and independent datasets (Fig. 5B). In addition, FFCM-MRF provided ~22X faster parameter tuning time on CPU compared to nnU-Net model training on GPU. The GPU inference time for nnU-Net (mean ± SD: 6.37 ± 2.67 s) was much less than FFCM-MRF (4.92 ± 1.90 min), which uses CPU, while the CPU inference time for nnU-Net (9.77 ± 3.02 min) is longer than FFCM-MRF (~2X, Supplementary Table 3). Although FFCM-MRF is not optimal in inference time compared with deep learning methods, we believe that FFCM-MRF is independent of high-performance graphic cards and minute-level processing time is acceptable in clinical application.

3.2. Ablation study

We also assessed the ablation models of FFCM-MRF. Specifically, we evaluated the performance of FFCM only, FFCM-MRF with energy function V_{c1}, FFCM-MRF with energy function V_{c2}, and FFCM-MRF with energy function $V_{c1} + V_{c2}$ (proposed). As shown in Table 4, the proposed FFCM-MRF achieved the highest DSC, precision, recall and ΔIslands,

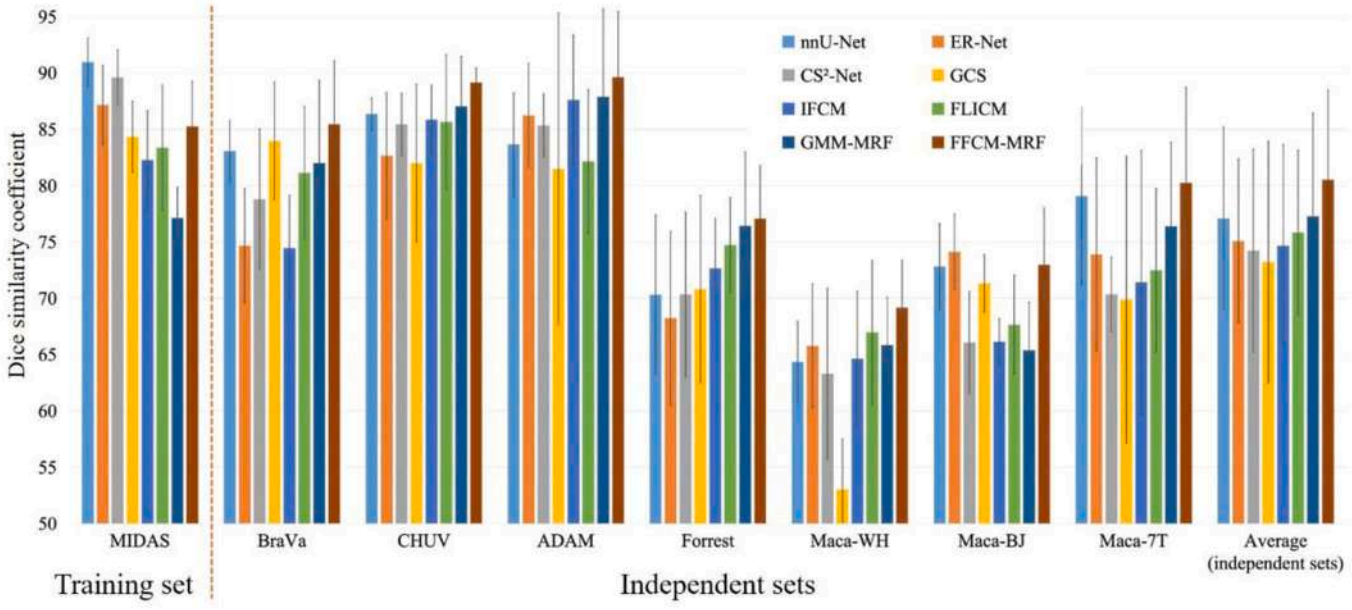

Fig. 2. Cerebrovascular segmentation results from eight different methods for both training and independent datasets were evaluated in terms of Dice similarity coefficient.

Table 3
Cerebrovascular segmentation results from eight different methods for each dataset in terms of Dice similarity coefficient (DSC), precision score, recall score, average Hausdorff distance (AHD), 95 % Hausdorff distance (95HD), ΔIslands and integrated rank metrics[a].

Datasets	Methods	DSC (%) ↑	Precision (%) ↑	Recall (%) ↑	AHD ↓	ΔIslands ↓	Integrated rank
MIDAS	nnU-Net	**90.96 (2.17)**	**93.18 (2.43)**	88.94 (3.63)	**0.25 (0.10)**	70.50 (22.86)	**1.4**
	ER-Net	87.16 (3.53)	92.34 (5.52)	83.44 (8.42)	0.40 (0.16)	104.17 (39.35)	3.6
	CS^2-Net	89.59 (2.45)	91.38 (3.24)	88.09 (4.56)	0.29 (0.11)	149.98 (48.32)	3.2
	GCS	84.33 (3.16)	82.99 (7.49)	86.65 (6.08)	0.46 (0.17)	350.69 (132.23)	5.4
	IFCM	82.28 (4.40)	92.57 (5.76)	75.01 (8.97)	0.64 (0.25)	211.22 (154.83)	5.8
	FLICM	83.36 (5.57)	89.59 (6.59)	79.32 (10.65)	0.46 (0.20)	255.56 (125.46)	5.8
	GMM-MRF	77.14 (2.70)	72.56 (4.81)	82.74 (4.14)	0.71 (0.22)	102.80 959.120	6.6
	FFCM-MRF (Proposed)	85.25 (3.99)	82.45 (8.46)	**89.05 (3.74)**	0.69 (0.33)	**39.85 (27.30)**	4.0
BraVa	nnU-Net	83.06 (2.72)	88.36 (9.17)	79.37 (7.10)	0.56 (0.27)	205.40 (23.83)	4.8
	ER-Net	74.68 (5.05)	**96.45 (4.17)**	61.35 (7.76)	0.92 (0.33)	106.40 (13.45)	5.0
	CS^2-Net	78.78 (6.25)	74.70 (12.63)	85.33 (6.03)	1.49 (0.91)	211.80 (50.58)	6.4
	GCS	83.97 (5.22)	93.74 (5.09)	77.00 (11.02)	**0.39 (0.29)**	174.80 (20.03)	3.4
	IFCM	74.46 (4.69)	89.76 (18.15)	68.62 (18.43)	1.08 (0.56)	122.80 (19.12)	6.2
	FLICM	81.14 (5.90)	96.04 (2.46)	70.81 (9.75)	0.46 (0.13)	97.00 (52.14)	3.6
	GMM-MRF	82.01 (7.34)	75.01 (13.34)	**92.70 (6.90)**	1.28 (0.79)	**34.00 (27.45)**	4.0
	FFCM-MRF	**85.45 (5.64)**	90.16 (9.14)	83.16 (13.56)	0.54 (0.22)	36.40 (20.43)	**2.6**
CHUV	nnU-Net	86.36 (1.44)	85.41 (5.94)	87.89 (5.00)	0.44 (0.08)	31.20 (10.40)	3.4
	ER-Net	82.66 (5.60)	75.72 (12.90)	93.16 (5.74)	0.65 (0.36)	126.40 (78.32)	6.0
	CS^2-Net	85.43 (2.77)	78.95 (5.54)	93.35 (1.54)	0.52 (0.22)	180.20 (48.47)	5.4
	GCS	82.01 (6.98)	71.70 (11.91)	**97.19 (1.72)**	0.95 (0.47)	183.20 (76.61)	6.6
	IFCM	85.86 (3.06)	80.27 (8.54)	93.16 (4.52)	0.45 (0.07)	53.40 (15.32)	4.0
	FLICM	85.65 (5.98)	83.48 (8.61)	89.41 (11.87)	0.48 (0.44)	92.60 (27.66)	5.0
	GMM-MRF	87.04 (4.42)	87.16 (13.56)	90.09 (13.47)	0.44 (0.19)	**28.00 (16.55)**	**2.4**
	FFCM-MRF	**89.16 (1.27)**	**92.54 (9.54)**	87.68 (10.40)	**0.37 (0.17)**	41.40 (36.17)	2.8
ADAM	nnU-Net	83.66 (4.57)	78.88 (10.47)	90.30 (4.47)	0.64 (0.10)	**21.20 (23.37)**	4.4
	ER-Net	86.23 (4.62)	84.12 (11.52)	90.01 (6.44)	0.47 (0.16)	90.40 (60.15)	4.0
	CS^2-Net	85.35 (2.79)	**92.60 (4.66)**	79.78 (7.99)	0.80 (0.32)	21.80 (12.40)	4.2
	GCS	81.49 (13.83)	82.37 (24.54)	87.05 (10.96)	1.27 (1.79)	112.30 (38.13)	7.2
	IFCM	87.62 (5.76)	87.06 (11.35)	90.29 (11.98)	0.60 (0.42)	100.80 (55.09)	4.0
	FLICM	82.15 (6.39)	92.15 (10.59)	77.01 (16.72)	0.86 (0.48)	113.80 (77.02)	6.4
	GMM-MRF	87.87 (7.82)	83.15 (16.78)	**95.70 (5.17)**	0.53 (0.31)	32.20 (21.57)	3.2
	FFCM-MRF	**89.63 (5.85)**	92.11 (10.56)	89.04 (12.01)	**0.34 (0.20)**	25.00 (17.20)	**2.6**
Forrest	nnU-Net	70.32 (7.08)	87.73 (4.23)	59.60 (10.26)	1.91 (0.70)	151.70 (109.50)	5.6
	ER-Net	68.24 (7.69)	89.13 (4.24)	56.22 (10.36)	2.37 (0.87)	**137.07 (112.42)**	5.6
	CS^2-Net	70.34 (7.32)	88.47 (3.84)	59.29 (10.32)	1.47 (0.46)	220.99 (104.54)	5.8
	GCS	70.82 (8.30)	**93.46 (3.08)**	57.89 (10.67)	1.14 (0.40)	178.57 (141.31)	4.8
	IFCM	72.65 (4.44)	89.79 (6.45)	61.40 (5.62)	1.06 (0.33)	175.56 (91.18)	3.6
	FLICM	74.71 (4.22)	87.84 (7.47)	65.32 (4.57)	1.08 (0.32)	235.80 (102.09)	4.6
	GMM-MRF	76.44 (6.57)	81.66 (7.62)	**73.70 (12.44)**	**0.81 (0.30)**	156.86 (123.64)	3.2
	FFCM-MRF	**77.06 (6.81)**	84.16 (6.58)	72.73 (12.45)	0.94 (0.35)	147.32 (96.99)	**2.8**
Maca-WH	nnU-Net	64.36 (3.62)	89.04 (4.67)	50.75 (5.31)	**0.92 (0.18)**	42.17 (17.36)	4.0
	ER-Net	65.77 (5.51)	74.87 (9.65)	59.17 (5.32)	1.41 (0.62)	72.67 (23.91)	5.4
	CS^2-Net	63.31 (7.60)	60.57 (11.44)	**67.41 (5.21)**	1.86 (0.81)	89.58 (18.34)	6.2
	GCS	53.02 (4.52)	**93.45 (3.04)**	37.21 (4.56)	1.82 (0.34)	30.31 (14.70)	5.0
	IFCM	64.62 (5.99)	77.03 (9.34)	56.73 (8.14)	1.33 (0.57)	43.67 (27.39)	5.0
	FLICM	66.97 (6.38)	78.68 (12.99)	60.01 (7.75)	1.25 (0.66)	40.62 (33.55)	3.0
	GMM-MRF	65.84 (4.26)	65.64 (6.36)	67.08 (8.26)	1.93 (0.85)	43.96 (13.92)	5.2
	FFCM-MRF	**69.16 (4.23)**	82.83 (8.10)	59.85 (4.97)	1.19 (0.42)	**18.17 (11.42)**	**2.2**
Maca-BJ	nnU-Net	72.81 (3.79)	65.49 (5.96)	**82.34 (3.05)**	3.32 (0.73)	194.25 (70.62)	5.4
	ER-Net	**74.12 (3.35)**	70.98 (4.98)	77.72 (3.35)	2.65 (0.56)	170.00 (43.41)	**3.8**
	CS^2-Net	66.07 (4.53)	52.90 (5.68)	**88.45 (2.51)**	4.19 (0.77)	123.00 (31.82)	5.8
	GCS	71.33 (2.56)	**84.95 (5.44)**	61.92 (6.09)	2.23 (0.51)	168.75 (47.10)	**3.8**
	IFCM	66.14 (2.06)	84.71 (10.18)	54.97 (5.59)	2.69 (0.45)	91.25 (52.10)	4.6
	FLICM	67.65 (4.40)	84.34 (6.45)	57.20 (7.85)	2.66 (0.81)	**85.25 (17.35)**	4.0
	GMM-MRF	65.39 (4.28)	66.20 (6.39)	65.37 (6.97)	**1.67 (0.46)**	98.75 (13.94)	4.8
	FFCM-MRF	72.97 (5.02)	66.96 (8.80)	80.89 (3.19)	3.07 (0.97)	94.25 (39.23)	**3.8**
Maca-7T	nnU-Net	79.07 (7.88)	73.12 (14.03)	**87.94 (5.53)**	**0.65 (0.37)**	106.75 (61.35)	**2.6**
	ER-Net	73.89 (8.57)	64.80 (14.40)	88.70 (7.17)	1.41 (0.89)	228.50 (195.52)	4.6
	CS^2-Net	70.35 (3.30)	57.44 (4.86)	91.21 (3.60)	1.84 (0.52)	294.00 (123.11)	6.4
	GCS	69.87 (12.74)	**88.61 (13.31)**	62.29 (22.64)	1.16 (0.45)	260.25 (138.40)	5.6
	IFCM	71.41 (11.71)	73.76 (12.27)	71.30 (16.98)	1.66 (0.56)	128.50 (41.35)	5.4
	FLICM	72.47 (7.27)	63.72 (12.71)	87.14 (9.05)	1.69 (0.53)	126.75 (93.04)	5.4
	GMM-MRF	76.40 (7.47)	70.54 (14.93)	86.16 (6.34)	0.92 (0.62)	**53.50 (43.87)**	3.2
	FFCM-MRF	**80.24 (8.52)**	78.71 (16.61)	83.98 (7.18)	1.01 (1.13)	60.50 (41.65)	2.8
Average (independent sets)	nnU-Net	77.09 (8.11)	81.15 (9.04)	76.88 (15.50)	1.21 (1.06)	107.52 (78.10)	4.43
	ER-Net	75.08 (7.28)	79.44 (11.00)	75.19 (16.02)	1.41 (0.83)	133.06 (52.78)	4.86
	CS^2-Net	74.23 (9.00)	72.23 (15.59)	80.69 (12.83)	1.74 (1.19)	163.05 (91.40)	7.29
	GCS	73.22 (10.72)	**86.9 (8.07)**	68.65 (20.05)	1.28 (0.60)	158.31 (71.07)	5.00
	IFCM	74.68 (8.96)	83.2 (6.32)	70.92 (15.39)	1.27 (0.75)	102.28 (45.51)	4.43

(*continued on next page*)

Table 3 (*continued*)

Datasets	Methods	DSC (%) ↑	Precision (%) ↑	Recall (%) ↑	AHD ↓	ΔIslands ↓	Integrated rank
	FLICM	75.82 (7.33)	83.75 (10.53)	72.41 (12.68)	1.21 (0.77)	113.12 (60.48)	4.29
	GMM-MRF	77.28 (9.16)	75.62 (8.57)	**81.54 (12.59)**	1.08 (0.57)	63.90 (47.52)	3.43
	FFCM-MRF	**80.52 (7.96)**	83.92 (9.10)	79.62 (10.21)	**1.07 (0.94)**	**60.43 (45.96)**	**1.29**

[a] Values are mean (SD) unless otherwise indicated. Bold denotes the best results from the eight different methods.

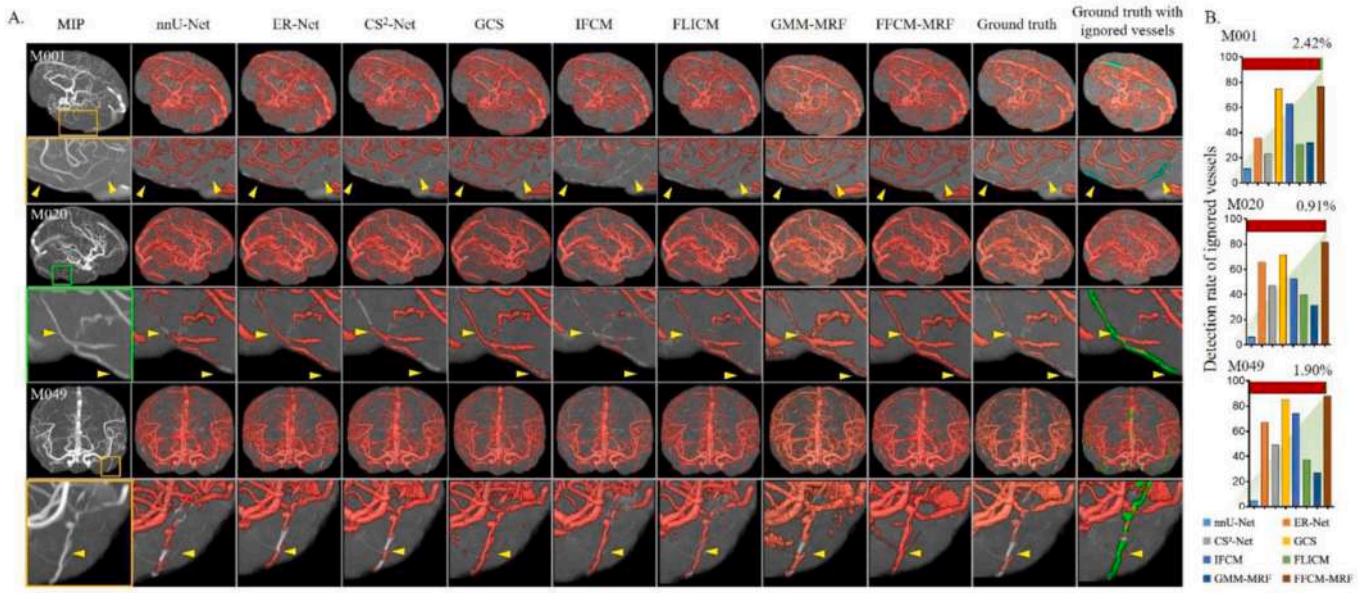

Fig. 3. Comparisons of the cerebrovascular segmentation results from the MIDAS dataset using state-of-the-art methods show that FFCM-MRF was superior in detecting ignored vessels. A, Left to right columns correspond to the maximum intensity projection (MIP) views for the TOF-MRA image, the results by nnU-Net, ER-Net, CS^2-Net, GCS, IFCM, FLICM, GMM-MRF, and FFCM-MRF, ground truth, and the ground truth with ignored vessels highlighted in green. Trained annotators meticulously delineated the ignored vessels for three subjects, as shown in the rightmost column in A. The yellow arrows indicate that FFCM-MRF can detect vessels that were not annotated in the ground truth. B, Detection rate of ignored vessels with state-of-the-art methods. Ignored vessels account for a small portion of the whole brain vessels in TOF-MRA, indicated by the green (ignored) and red (ground truth) colors of the horizontal bars in B. The bar plots indicate that FFCM-MRF was superior in detecting the ignored vessels.

demonstrating that it has the capability to suppress segmentation noise and improve segmentation accuracy.

3.3. Test-retest reliability

The reliability of the vascular volume density and average diameter using the human Brainnetome atlas is shown in Fig. 6A and Supplementary Table 4. Most regions exhibited good (0.72–0.90) to excellent (>0.90) ICC values across four scans with the exception of the middle temporal gyrus and lateral occipital cortex in volume density. The diameters showed less reliability than the volume densities. Across subjects, the average ICCs were 0.996 and 0.863 for the total brain vascular volume and average within-brain diameter, respectively (Supplementary Figure 8). A comparison of vascular volume density and diameter by the macaque Brainnetome atlas between two 3 T scans from a single subject is shown in Fig. 6B. The intra-subject results show that FFCM-MRF provides highly consistent measures of vascular morphology. Fig. 6C shows the differences between 3 T and 7 T scans from a macaque. We observed that the vessels detected from 7 T MRA appeared denser compared to those identified by 3 T MRA. The average diameter from 7 T was smaller than those from 3 T, indicating that 7 T MRA can detect more slender vessels.

3.4. FFCM-MRF application

ROI-based and voxelwise group-averaged vascular volume density and diameter maps across the cortex for humans and macaques are shown in Fig. 7 and Supplementary Figure 9. The patterns of vascular volume density and diameter were consistent across species, with dense and large arteries in the insular and anterior cingular regions and sparse and slender arteries in the lateral occipital region, indicating that the vascular pattern was highly conserved during evolution.

4. Discussion

In the present study, we developed a fully automatic unsupervised cerebrovascular segmentation method, FFCM-MRF, which integrated fast FCM clustering with MRF optimization by utilizing shape priors and spatial constraints. Compared with state-of-the-art deep learning and statistical model-based methods, this approach is highly accurate and reliable and largely independent of field strength, scanner types, acquisition parameters, and species.

Statistical model combined with MRF models for cerebrovascular segmentation has been reported previously [11–13]. Most studies utilized finite mixture models to fit the intensity distribution of TOF-MRA data, and expectation maximization algorithm was used to estimate the parameters. In contrast, this study used the FFCM algorithm, which is unaffected by extremely small proportion of cerebral vessels. In addition, we designed a novel energy function incorporating vessel shape priors for MRF model to reduce noise and improve segmentation performance. Compared with the GMM-MRF [11], FFCM-MRF achieved an average increase of 3.24 % in DSC across multiple human and macaque datasets, and was capable of effectively suppressing noise. Quantitative comparisons among FLICM, IFCM and FFCM-MRF showed that

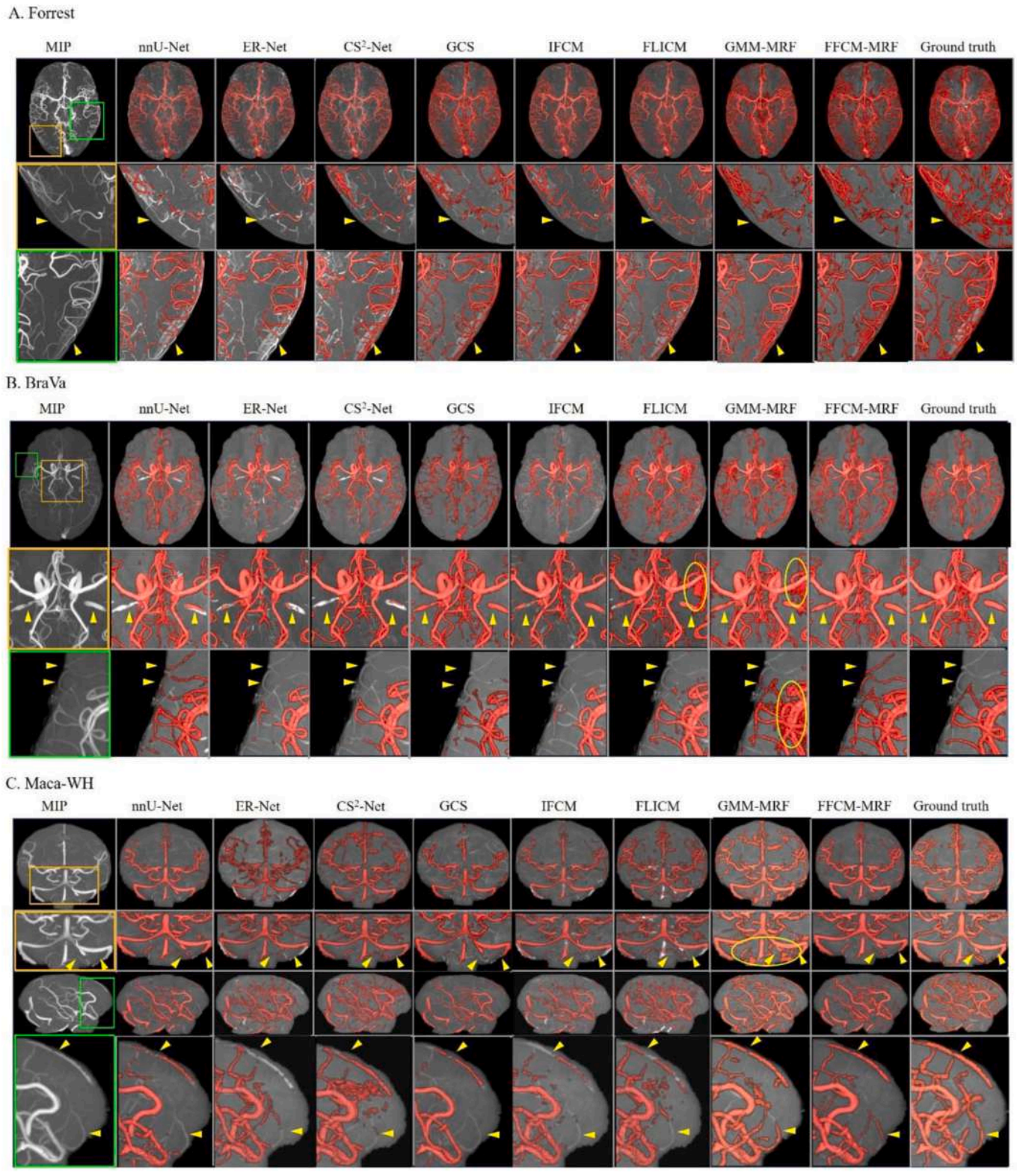

Fig. 4. Qualitative comparisons of the cerebrovascular segmentation results from independent datasets using state-of-the-art methods. Left to right columns correspond to a maximum intensity projection (MIP) view for the TOF-MRA image, results by nnU-Net, ER-Net, CS^2-Net, GCS, IFCM, FLICM, GMM-MRF, and FFCM-MRF as well as the ground truth. Yellow arrows indicate that deep learning models performed poorly on the Forrest (A), BraVa (B) and Maca-WH (C) datasets for large arteries (B) and small distal vessels (A, B, and C). Yellow ellipses show that FFCM-MRF was more robust to noise than FLICM and GMM-MRF.

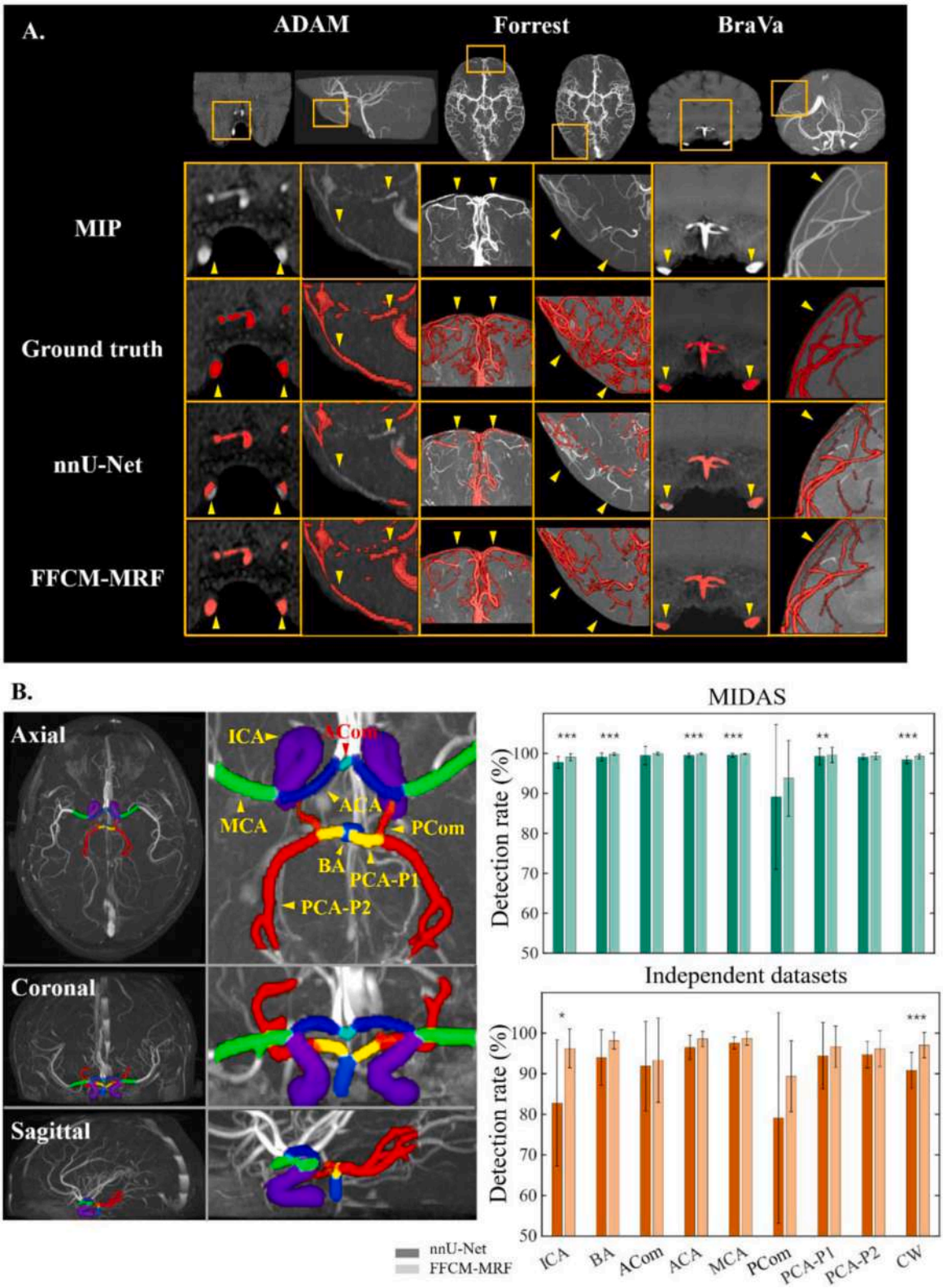

Fig. 5. Comparison of segmentation results between nnU-Net and FFCM-MRF. A, Vessels near the edge of the brain/image, including major large vessels at the base of the brain and small distal arteries covering the cerebral cortical surface, were not well segmented by nnU-Net. Note that the ADAM MRA images only partially covered the brain. B, Comparison of nnU-Net and FFCM-MRF in segmenting the Circle of Willis (CW). CW arteries were labeled using Dumais et al. (2022). Bar plots showing the proportion of segmented vessels in each CW artery and in the total CW using nnU-Net and FFCM-MRF. The Forrest MRA data only partially covered the CW and were not labeled in this study. ACA, anterior cerebral artery; ACom, anterior communicating artery; BA, basilar artery; ICA, internal carotid artery; MCA, middle cerebral artery; PCA, posterior cerebral artery; PCom, posterior communicating artery. Paired t tests with Bonferroni correction were performed between nnU-Net and FFCM-MRF. ***, corrected $p < .001$; **, corrected $p < .01$; *, corrected $p < .05$.

Table 4
Cerebrovascular segmentation results from ablation models of FFCM-MRF on MIDAS dataset.

Models	DSC (%) ↑	Precision (%) ↑	Recall (%) ↑	AHD ↓	ΔIslands ↓	Integrated rank
FFCM	82.27 (5.30)	78.29 (10.75)	88.15 (5.16)	0.83 (0.47)	116.94 (72.61)	6.0
FFCM-MRF ($U = V_{c1}$)	83.98 (4.17)	81.50 (9.27)	87.76 (5.31)	**0.68 (0.33)**	39.52 (26.89)	4.0
FFCM-MRF ($U = V_{c2}$)	83.94 (4.07)	81.84 (9.26)	87.29 (5.43)	0.69 (0.33)	**39.44 (27.36)**	4.4
FFCM-MRF ($U = V_{c1}+V_{c2}$)	**85.25 (3.99)**	**82.45 (8.46)**	**89.05 (3.74)**	0.69 (0.33)	39.85 (27.30)	**3.4**

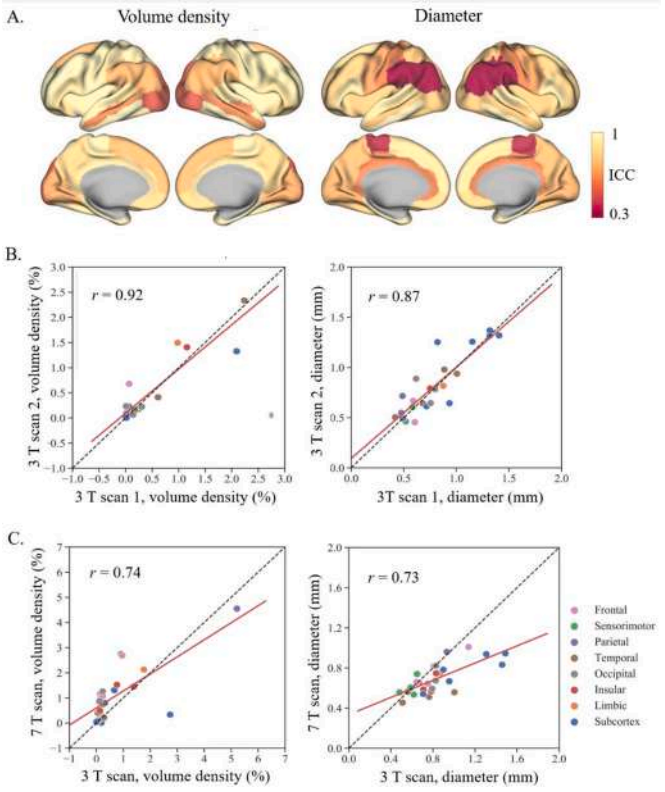

Fig. 6. Test-retest results of region-specific volume density (left) and average diameter (right) for humans (A) and macaques (B, C). A, Intraclass correlation coefficient (ICC) overlaid on the human Brainnetome atlas for subjects in the MSC dataset. B and C, Interscan reliability based on the macaque Brainnetome atlas in two 3 T scans and in 3 T and 7 T scans in one macaque. The red line represents the best linear fit of the correlation between the measurements from two scans. The black dotted line represents a hypothetical complete agreement between the measurements from the two scans.

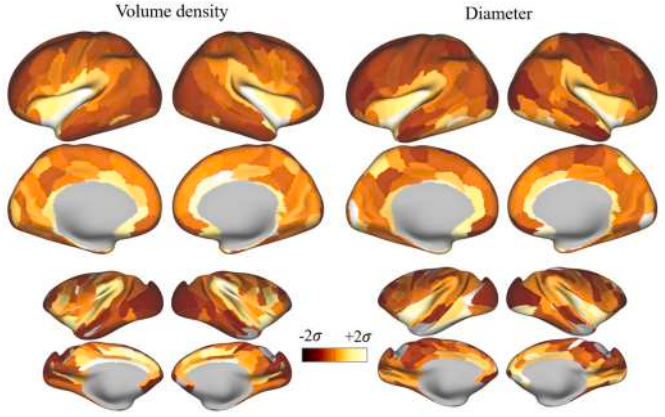

Fig. 7. Group-averaged cerebrovascular volume density and diameter for humans and rhesus monkeys. Human and rhesus monkey Brainnetome atlases were used to extract the ROI-based vascular features.

FFCM-MRF outperformed FLICM and IFCM in terms of DSC across all datasets, verifying that the proposed method is highly accurate and robust compared with FCM-type of methods. In addition, we found that the FFCM-MRF method has the lowest time complexity among the statistical model-based methods, suggesting the high computational efficiency of FFCM-MRF (for details refer to the supplementary file). Deep learning techniques have made rapid progress in cerebrovascular segmentation [3,4,23,34]. However, most cross-validation strategies were based on the same dataset [5,6]. A variety of scanners, acquisition protocols and species pose challenges for independent replications. We found that the proposed FFCM-MRF outperformed Transformer-based semi-supervised model GCS in all datasets with an average increase of 7.3 % in DSC for humans and macaques. nnU-Net, ER-Net and CS^2-Net outperformed FFCM-MRF in the dataset for model training (i.e., MIDAS); however, FFCM-MRF improved the segmentation performance in all the independent datasets by increased DSC scores for humans and macaques (Fig. 2). Given that diverse datasets covering a wider range were tested, it is reasonable to conclude that FFCM-MRF is capable of generalizing to new TOF-MRA data. The proposed method self-adaptively discriminates between vessel and non-vessel voxels based on intensity contrasts of the image. As shown in Supplementary Figure 10, although the voxel intensity distributions were different between humans and monkeys, the vessel and non-vessel voxels exhibited well-isolated distributions in both species and could be identified and utilized for discrimination by FFCM. It is for this reason that vascular anatomical structural differences between humans and macaques (e.g., the lack of an anterior communicating artery in rhesus monkeys) do not affect segmentation results for rhesus monkeys. Rhesus monkeys are vital animal models in developing therapeutics for brain diseases. To the best of our knowledge, our work is the first to generalize cerebrovascular segmentation algorithms to nonhuman primates. The effectiveness of FFCM-MRF for macaque cerebrovascular segmentation may promote progress in comparative neuroscience and translational medicine.

Because the vasculature annotations shown are voxel-based delineations on three views of 2D slices of TOF-MRA as shown in Supplementary Figure 11, the tubular and continuous shape information about the vessels was always cut into cross-sections. Without 3D intuitionistic vascular shape information, oversights always exist, especially for small distal arteries even if the annotator has experience and anatomical knowledge of the vascular system. Manual labeling of the whole brain's sophisticated and complex vasculature network is therefore subjective, time-consuming, and prone to inter-subject variability. In addition to generalizability, FFCM-MRF has unique superiority in detecting vessels that are ignored by annotators because it does not rely on ground truth labels. In contrast, deep learning models learn vascular representations depending on large-scale high-quality ground truth labels, so the segmentation results may be compromised due to the inaccurate or insufficient annotations.

Qualitative comparisons between nnU-Net and FFCM-MRF showed that vessels near the edge of the brain/image, including major large vessels in the CW at the base of the brain and small distal arteries that cover the cerebral cortical surface, were often poorly detected by nnU-Net. Quantitative analyses of the CW arterial segmentations demonstrated that FFCM-MRF was more effective in segmenting the CW across all datasets, indicating that the proposed method is robust and superior for CW segmentation. Stenosis of the CW arteries restricts the passage of blood and significantly increases the risk of stroke [35], cognitive

impairment [36,37], and Alzheimer's disease [38] and increases the risk of progression from mild cognitive impairment to dementia [39]. For these reasons, accurate segmentation of the CW is essential for early identification of cerebrovascular and neurodegenerative diseases.

Compared with 3 T MRA, high field strength 7 T MRA performs better in terms of signal-to-noise and contrast-to-noise ratio [40]. Our model showed the best Dice scores for the 7 T human and macaque datasets compared with state-of-the-art methods and detected more slender vessels than using 3 T TOF-MRA. We observed that the segmentation accuracy for the 7 T Forrest dataset was poorer than for the other human 3 T datasets. It is possible that the ground truth labels contained noise and thus compromised the segmentation performance for this dataset (Fig. 4A). Test-retest results showed that FFCM-MRF is robust and replicable with good intra-subject results in terms of arterial localization and structural morphology. Reliable and generalizable results suggest that the FFCM-MRF model has the potential to facilitate the use of an automated vascular identification system in real-world research and clinical environments with their heterogeneity in scanners and subjects.

In the process of brain development, vessels act as a powerful signaling system that mediates and guides cell migration, differentiation, and structural connectivity during the development of neurons and glial cells [41]. This neurovascular interaction established during development continues to play a fundamental role in communication between the vascular and nervous systems throughout adulthood [42]. Evidence has shown that morphological vascular features, such as volume and diameter, are interregionally heterogeneous across the brain [20,21,43] and are correlated with distinct neurons [43]. Consistent with previous reports [20], the present study found various distributions of the volume density and lumen diameter of cortical arteries in humans, with dense and large cerebral arteries in the insular and anterior cingular regions and sparse and slender arteries in the lateral occipital area. Similar vascular patterns were found in rhesus monkeys in the present study. Previous findings have reported dense cerebrovascular networks in the primary sensory cortices in mice [43]. However, we found that the primary sensory cortices had a medium vascular density in humans and macaques. It is possible that the mice studies included the whole vasculature network, which contains arteries, veins and capillaries using immunofluorescence staining or tissue transparency techniques. In contrast, in vivo TOF-MRA can image arteries and part of the veins at hundreds of micrometer resolution. Another explanation may be that there are dramatic differences in brain organization between rodents and primates. To our knowledge, this work is the first in which human and macaque vascular structures were extracted in vivo and showed that brain-specific vascularization distributions are highly conserved across primates. Accurate cerebrovascular segmentation for humans and macaques will provide benefits in understanding the evolution and pathophysiological underpinnings of diseases.

TOF-MRA allows for three-dimensional visualization and morphology quantification of the intracranial vessels in vivo and has become a powerful tool available in research and clinical settings. Robust, generalized and open-access tools, such as FFCM-MRF, have the potential to harmonize and process data from different sites, which represent real-world environments with their heterogeneity in participants and scanners. Although some semi-automated GUI tools have been developed, they are not publicly available [44], or they utilize traditional region-based/level set methods requiring heavy manual interventions [45]. As of yet, there is no user-friendly open-source toolbox for automated cerebrovascular segmentation and analysis. The present study integrated FFCM-MRF framework along with morphometric feature extraction functions into a user-friendly GUI toolbox (Supplementary files and a manual in the appendix) and is freely available at GitHub repository https://github.com/YueCui-Labs/FFCM-MRF. It was developed in MATLAB (MathWorks, Inc.) and consists of TOF-MRA preprocessing, vascular segmentation, feature extraction and quantification. Currently, there is also a lack of publicly available rhesus monkey angiography datasets. Macaque data from the Maca-7T and Maca-BJ datasets along with ground truth labels will be released on the OpenNeuro platform (https://openneuro.org) to promote the development of cutting-edge algorithms that can enable cerebrovascular segmentation and analysis across species.

5. Conclusions

This study proposed FFCM-MRF, an automated and open-source method for accurate intracranial cerebrovascular segmentation. The results demonstrated the superiority of our developed framework for brain vessel segmentation and its ability to generalize well to multiple human and macaque datasets. Because it can provide accurate regional features from segmentation, FFCM-MRF can facilitate the study of novel imaging biomarkers for cerebrovascular and neurodegenerative diseases, and thereby enable diagnoses and preventative treatments as early as possible.

Funding

This work was supported by STI 2030 - Major Projects (No. 2021ZD0200402) and National Science Foundation of China (No. 82371486).

Data/code availability

All TOF-MRA data used to develop and validate FFCM-MRF were acquired from different public human (MIDAS, BraVa, CHUV, ADAM, Forrest and MSC) and private macaque datasets (Maca-WH, Maca-BJ and Maca-7T). Macaque TOF-MRA data and ground truth labels from the Maca-BJ and Maca-7T have been released via OpenNeuro: https://openneuro.org/datasets/ds004620/versions/1.0.0. Data from the Maca-WH can be obtained upon reasonable request. URL links for public datasets are:

- MIDAS: https://public.kitware.com/Wiki/TubeTK/Data
- BraVa: http://cng.gmu.edu/brava/home.php
- CHUV: https://openneuro.org/datasets/ds003949/versions/1.0.1
- ADAM: https://adam.isi.uu.nl/
- Forrest: https://openneuro.org/datasets/ds000113/versions/1.3.0
- MSC: https://legacy.openfmri.org/dataset/ds000224/

FFCM-MRF pipeline GitHub repository: https://github.com/YueCui-Labs/FFCM-MRF.

CRediT authorship contribution statement

Yue Cui: Conceptualization, Data curation, Funding acquisition, Investigation, Methodology, Validation, Writing – original draft, Writing – review & editing. **Haibin Huang:** Investigation, Methodology, Validation, Visualization, Writing – original draft, Writing – review & editing. **Jialu Liu:** Investigation, Methodology, Visualization. **Mingyang Zhao:** Conceptualization, Methodology, Writing – original draft. **Chengyi Li:** Investigation, Methodology, Writing – original draft. **Xinyong Han:** Methodology, Resources, Writing – original draft. **Na Luo:** Methodology, Resources, Writing – original draft. **Jinquan Gao:** Resources, Validation. **Dong-Ming Yan:** Methodology, Resources, Writing – original draft. **Chen Zhang:** Resources, Validation, Writing – original draft. **Tianzi Jiang:** Data curation, Validation, Writing – original draft. **Shan Yu:** Conceptualization, Data curation, Funding acquisition, Investigation, Methodology, Resources, Supervision, Validation, Visualization, Writing – original draft, Writing – review & editing.

Declaration of competing interest

The authors declare that they have no known competing financial

interests or personal relationships that could have appeared to influence the work reported in this paper.

Acknowledgements

This work was supported by STI 2030 - Major Projects (No. 2021ZD0200402) and National Natural Science Foundation of China (No. 82371486).

Appendix A. Supplementary data

Supplementary data to this article can be found online at https://doi.org/10.1016/j.compbiomed.2024.107996.

References

[1] M.D. Sweeney, K. Kisler, A. Montagne, A.W. Toga, B.V. Zlokovic, The role of brain vasculature in neurodegenerative disorders, Nat. Neurosci. 21 (2018) 1318–1331.
[2] D.C. Van Essen, C.J. Donahue, T.S. Coalson, H. Kennedy, T. Hayashi, M.F. Glasser, Cerebral cortical folding, parcellation, and connectivity in humans, nonhuman primates, and mice, Proc. Natl. Acad. Sci. USA 116 (2019) 26173–26180.
[3] M. Livne, J. Rieger, O.U. Aydin, A.A. Taha, E.M. Akay, T. Kossen, J. Sobesky, J. D. Kelleher, K. Hildebrand, D. Frey, A U-Net deep learning framework for high performance vessel segmentation in patients with cerebrovascular disease, Front. Neurosci. 13 (2019) 97.
[4] F. Isensee, P.F. Jaeger, S.A. Kohl, J. Petersen, K.H. Maier-Hein, nnU-Net: a self-configuring method for deep learning-based biomedical image segmentation, Nat. Methods 18 (2021) 203–211.
[5] Q. Wu, Y. Chen, N. Huang, X. Yue, Weakly-supervised cerebrovascular segmentation network with shape prior and model indicator, Proc. Int. Congr. Ment. Retard. (2022) 668–676.
[6] C. Chen, K. Zhou, Z. Wang, R. Xiao, Generative consistency for semi-supervised cerebrovascular segmentation from TOF-MRA, IEEE Trans. Med. Imag. 42 (2023) 346–353.
[7] L. Xia, H. Zhang, Y. Wu, R. Song, Y. Ma, L. Mou, J. Liu, Y. Xie, M. Ma, Y. Zhao, 3D vessel-like structure segmentation in medical images by an edge-reinforced network, Med. Image Anal. 82 (2022) 102581.
[8] L. Mou, Y. Zhao, H. Fu, Y. Liu, J. Cheng, Y. Zheng, P. Su, J. Yang, L. Chen, A. F. Frangi, CS2-Net: deep learning segmentation of curvilinear structures in medical imaging, Med. Image Anal. 67 (2021) 101874.
[9] A. Vaswani, N. Shazeer, N. Parmar, J. Uszkoreit, L. Jones, A.N. Gomez, Ł. Kaiser, I. Polosukhin, Attention is all you need, Adv. Neural Inf. Process. Syst. 30 (2017).
[10] S. Moccia, E. De Momi, S. El Hadji, L.S. Mattos, Blood vessel segmentation algorithms—review of methods, datasets and evaluation metrics, Comput. Methods Progr. Biomed. 158 (2018) 71–91.
[11] B. Zhang, Z. Wu, S. Liu, S. Zhou, N. Li, G. Zhao, A Device-independent Novel Statistical Modeling for Cerebral TOF-MRA Data Segmentation, Uncertainty for Safe Utilization of Machine Learning in Medical Imaging and Clinical Image-Based Procedures, 2019, pp. 172–181.
[12] Z. Lv, F. Mi, Z. Wu, Y. Zhu, X. Liu, M. Tian, F. Zhang, X. Wang, X. Wan, A parallel cerebrovascular segmentation algorithm based on focused multi-Gaussians model and heterogeneous Markov random field, IEEE Trans. NanoBioscience 19 (2020) 538–546.
[13] L. Wen, X. Wang, Z. Wu, M. Zhou, J.S. Jin, A novel statistical cerebrovascular segmentation algorithm with particle swarm optimization, Neurocomputing 148 (2015) 569–577.
[14] M.J. Christ, R. Parvathi, Fuzzy c-means algorithm for medical image segmentation, in: 3rd IEEE International Conference on Electronics Computer Technology, 2011, pp. 33–36.
[15] S. Krinidis, V. Chatzis, A robust fuzzy local information C-means clustering algorithm, IEEE Trans. Image Process. 19 (2010) 1328–1337.
[16] S. Shen, W. Sandham, M. Granat, A. Sterr, MRI fuzzy segmentation of brain tissue using neighborhood attraction with neural-network optimization, IEEE Trans. Inf. Technol. Biomed. 9 (2005) 459–467.
[17] J. Hao, J. Zhao, M. Li, Spatial continuity incorporated multi-attribute fuzzy clustering algorithm for blood vessels segmentation, Sci. China Inf. Sci. 53 (2010) 752–759.
[18] J. Yang, S. Ma, W. Tan, Q. Sun, P. P Cao, D. Zhao, MRA fuzzy c-means vessel segmentation algorithm based on tubular structure, J. Med. Imaging Health Inform. 5 (2015) 1853–1858.
[19] T. Jerman, F. Pernuš, B. Likar, Ž. Špiclin, Enhancement of vascular structures in 3D and 2D angiographic images, IEEE Trans. Med. Imag. 35 (2016) 2107–2118.
[20] M. Bernier, S.C. Cunnane, K. Whittingstall, The morphology of the human cerebrovascular system, Hum. Brain Mapp. 39 (2018) 4962–4975.
[21] C. Kirst, S. Skriabine, A. Vieites-Prado, T. Topilko, P. Bertin, G. Gerschenfeld, F. Verny, P. Topilko, N. Michalski, M. Tessier-Lavigne, Mapping the fine-scale organization and plasticity of the brain vasculature, Cell 180 (2020) 780–795.
[22] S.N. Wright, P. Kochunov, F. Mut, M. Bergamino, K.M. Brown, J.C. Mazziotta, A. W. Toga, J.R. Cebral, G.A. Ascoli, Digital reconstruction and morphometric analysis of human brain arterial vasculature from magnetic resonance angiography, Neuroimage 82 (2013) 170–181.
[23] F. Dumais, M.P. Caceres, F. Janelle, K. Seifeldine, N. Arès-Bruneau, J. Gutierrez, C. Bocti, K. Whittingstall, eICAB: a novel deep learning pipeline for Circle of Willis multiclass segmentation and analysis, Neuroimage 260 (2022) 119425.
[24] A. Hilbert, V.I. Madai, E.M. Akay, O.U. Aydin, J. Behland, J. Sobesky, I. Galinovic, A.A. Khalil, A.A. Taha, J. Wuerfel, BRAVE-NET: fully automated arterial brain vessel segmentation in patients with cerebrovascular disease, Frontiers in Artificial Intelligence 3 (2020) 552258.
[25] Y Cui, H Huang, J Gao, T Jiang, C Zhang, S Yu, Mapping blood traits to structural organization of the brain in rhesus monkeys, Cerebral Cortex 33 (2) (2023) 247–257.
[26] S.M. Smith, Fast robust automated brain extraction, Hum. Brain Mapp. 17 (2002) 143–155.
[27] X. Wang, X.-H. Li, J.W. Cho, B.E. Russ, N. Rajamani, A. Omelchenko, L. Ai, A. Korchmaros, S. Sawiak, R.A. Benn, U-net model for brain extraction: trained on humans for transfer to non-human primates, Neuroimage 235 (2021) 118001.
[28] S. Moussa, S. Chouaib, Brain MRI segmentation using a fast fuzzy c-means algorithm, in: 4th IEEE International Symposium on Informatics and its Applications (ISIA), 2020, pp. 1–6.
[29] J. Besag, Spatial interaction and the statistical analysis of lattice systems, Journal of the Royal Statistical Society: Series B (Methodological) 36 (2) (1974) 192–225.
[30] M.S. Hassouna, A.A. Farag, S. Hushek, T. Moriarty, Cerebrovascular segmentation from TOF using stochastic models, Medical image analysis 10 (1) (2006) 2–18.
[31] L. Fan, H. Li, J. Zhuo, Y. Zhang, J. Wang, L. Chen, Z. Yang, C. Chu, S. Xie, A. R. Laird, P.T. Fox, S.B. Eickhoff, C. Yu, T. Jiang, The human brainnetome atlas: a new brain atlas based on connectional architecture, Cerebr. Cortex 26 (2016) 3508–3526.
[32] Y. Lu, Y. Cui, L. Cao, L. Cheng, C. Wang, Y. Liu, B. Zhang, H. Wang, K. Li, L. Ma, Macaque Brainnetome Atlas: A Multifaceted Brain Map with Parcellation, Connection, and Histology, bioRxiv (2022), https://doi.org/10.1101/2022.10.18.512488.
[33] A. Bizeau, G. Gilbert, M. Bernier, M.T. Huynh, C. Bocti, M. Descoteaux, K. Whittingstall, Stimulus-evoked changes in cerebral vessel diameter: a study in healthy humans, J. Cerebr. Blood Flow Metabol. 38 (2018) 528–539.
[34] V.N. Dang, F. Galati, R. Cortese, G. Di Giacomo, V. Marconetto, P. Mathur, K. Lekadir, M. Lorenzi, F. Prados, M.A. Zuluaga, Vessel-CAPTCHA: an efficient learning framework for vessel annotation and segmentation, Med. Image Anal. 75 (2022) 102263.
[35] K. Malhotra, J. Gornbein, J.L. Saver, Ischemic strokes due to large-vessel occlusions contribute disproportionately to stroke-related dependence and death: a review, Front. Neurol. 8 (2017) 651.
[36] M.J.R. Lim, C.S. Tan, B. Gyanwali, C. Chen, S. Hilal, The effect of intracranial stenosis on cognitive decline in a memory clinic cohort, Eur. J. Neurol. 28 (2021) 1829–1839.
[37] M.F.K. Suri, J. Zhou, Y. Qiao, H. Chu, A.I. Qureshi, T. Mosley, R.F. Gottesman, L. Wruck, A.R. Sharrett, A. Alonso, Cognitive impairment and intracranial atherosclerotic stenosis in general population, Neurology 90 (2018) e1240–e1247.
[38] Z. Arvanitakis, A.W. Capuano, S.E. Leurgans, D.A. Bennett, J.A. Schneider, Relation of cerebral vessel disease to Alzheimer's disease dementia and cognitive function in elderly people: a cross-sectional study, Lancet Neurol. 15 (2016) 934–943.
[39] J. Zhu, Y. Wang, J. Li, J. Deng, H. Zhou, Intracranial artery stenosis and progression from mild cognitive impairment to Alzheimer disease, Neurology 82 (2014) 842–849.
[40] Z. Shi, X. Zhao, S. Zhu, X. Miao, Y. Zhang, S. Han, B. Wang, B. Zhang, X. Ye, Y. Dai, Time-of-Flight intracranial MRA at 3 T versus 5 T versus 7 T: visualization of distal small cerebral arteries, Radiology 306 (2023) 207–217.
[41] M. Segarra, M.R. Aburto, J. Hefendehl, A. Acker-Palmer, Neurovascular interactions in the nervous system, Annu. Rev. Cell Dev. Biol. 35 (2019) 615–635.
[42] P.J. Drew, Neurovascular coupling: motive unknown, Trends Neurosci. 45 (2022) 809–819.
[43] Y.-t. Wu, H.C. Bennett, U. Chon, D.J. Vanselow, Q. Zhang, R. Muñoz-Castañeda, K. C. Cheng, P. Osten, P.J. Drew, Y. Kim, Quantitative relationship between cerebrovascular network and neuronal cell types in mice, Cell Rep. 39 (2022) 110978.
[44] L. Chen, M. Mossa-Basha, N. Balu, G. Canton, J. Sun, K. Pimentel, T.S. Hatsukami, J.N. Hwang, C. Yuan, Development of a quantitative intracranial vascular features extraction tool on 3 D MRA using semiautomated open-curve active contour vessel tracing, Magn. Reson. Med. 79 (2018) 3229–3238.
[45] R. Izzo, D. Steinman, S. Manini, L. Antiga, The vascular modeling toolkit: a python library for the analysis of tubular structures in medical images, J. Open Source Softw. 3 (2018) 745.